



Experimental study and numerical simulation of three dimensional two-phase impinging jet flow using anisotropic turbulence model

Hamid Reza Nazif*

Department of Mechanical Engineering, Imam Khomeini International University, Qazvin, Iran

Article info:

Type: Research
Received: 11/10/2017
Revised: 15/10/2018
Accepted: 25/10/2018
Online: 27/10/2018

Keywords:

Impinging jet,
Anisotropy turbulence,
Wall function,
Two-phase flow.

Abstract

Hydrodynamic of a turbulent impinging jet on a flat plate is studied experimentally and numerically. Experiments are conducted for the Reynolds number range of 72000 to 102000 and a fixed jet-to-plate dimensionless distance of $H/d=3.5$. Based on the experimental setup, a multi-phase numerical model is simulated to predict the flow properties of impinging jets using two turbulent models. Mesh-independency of the numerical model is studied to ensure the preciseness of the results. Numerical and experimental forces on the target plate are compared in order to examine the performance of turbulent models and wall functions. As a result, the force obtained by the Reynolds stress turbulent model alongside with non-equilibrium wall function is in good agreement with the experiment. The correlation equations are obtained for predicting the water thickness over the target plate and impingement force versus Reynolds number. It is also indicated that the maximum shear stress on the target plate is located at radial dimensionless distance of $r/d=0.75$.

1. Introduction

Impinging jet is a practical phenomenon in many fields such as surface cleaning, drilling, cooling systems, temperature control in materials processing, etc. The required performance can be optimized by perfectly anticipating special characteristics of impinging jet flows. The fluid flow developed by a liquid jet impacting on a hot surface represents a complex physical problem governed by various interacting parameters, e.g. jet diameter, jet velocity, Reynolds number, Prandtl number, distance of the nozzle to the plate, surface temperature, roughness, and liquid properties including surface tension. Steady state stream of impinging jet creates three main regions through the flow including free jet

region, impingement region (also called stagnation region) and wall jet region [1]. Fluid flow exit from nozzle makes a fluid column called the free jet region. Impingement of free jet on a surface increases the pressure of the fluid. This high pressure region is called impingement region. With fluid departure from this region, its kinetic energy is increased and flow spreads over the surface. This part of the stream which includes flow over the target surface is called wall jet region.

In some studies, impinging jet flow and heat transfer features have been investigated by experimental approaches [2-6]. Cooper et al. [2] had a detailed look at impinging jet flow properties. Lee et al. [3] investigated the effects

*Corresponding author
email address: nazif@eng.ikiu.ac.ir

of nozzle diameter on impinging jet flow and heat transfer. Alekseenko and Markovich [4] had a precise look at shear stress on the surface. The effects of impinging inclination on local Nusselt number and surface pressure distribution were determined by Akansu et al. [5] for an impinging air flow. Meslem et al. [6] compared some properties of impinging jets such as velocity and wall shear stress for two different nozzle types.

A number of studies solved impinging jets analytically in addition to the experimental method [7-9]. Stevens and Webb [7] investigated radial velocity profile in the wall jet region. Modak et al. [8] and Katti and Prabhu [9] measured the Nusselt number on the surface in experimental and analytical approaches. Furthermore, Katti and Prabhu [9] conducted their studies for different H/d distances.

With increase in computer powers and development of numerical methods, many phenomena can be modeled. The complicated fluid flow in impinging jets can be simulated as well. Some studies have tried to introduce suitable turbulent models for impinging jets [10-12]. Coussirat et al. [10] compared one- and two equation models with experimental data in a two dimensional and single phase model. Performance of four turbulent models (three Reynolds Stress and one $k-\epsilon$) on modeling turbulent impinging jet flow was studied by Craft et al. [11]. Zuckerman and Lior [12] first examined the performance of five different turbulent models in simulating a two dimensional single phase impinging jet on a flat surface by using the published test data, and chose the v^2f model as a capable turbulent model for this purpose. Later, they investigated jet impingement flow and heat transfer on a cylindrical target.

Nasif et al. [13] simulated a three dimensional impinging jet and studied its heat transfer in a confined space. One of the applications of these jets in confined spaces is drill and work piece cooling while drilling process. Therefore, Schuler et al. [14] investigated confined impinging jet heat transfer in supercritical pressures. Heat transfer and phase interface were investigated for an impinging water jet by Hosain et al. [15]. They applied VOF multiphase model alongside the realizable $k-\epsilon$ turbulent

model to three- and two-dimensional geometries. Pakhomov and Terekhov [16] simulated a two-dimensional intermittent impinging jet.

In many studies on impinging jets, experimental data are used as a measure for numerical results validation [17-21]. Shademan et al. [17] simulated single-phase impinging jet in a three-dimensional model for a high H/d distance ($H/d=20$). They compared centerline velocity and surface pressure with previous experimental data by using the LES turbulent model. In another research, Wienand et al. [18] investigated flow properties for varying jet-to-plate distances of $H/d = \{2; 6; 10; 14\}$ by using a two-dimensional geometry and compared results with literature data. Also, Simionescu et al. [19] compared vortices made by laminar impinging air jets in a computational method with their own experimental data. Jet impingement heat transfer for low and median jet-to-plate distances ($H/d < 9$) was studied by Eschmann et al. [20] in numerical and experimental methods. Also, Ahmed et al. [21] conducted experiments for swirling turbulent impinging jets. In addition, with a focus on the effect of swirling speed on heat transfer, they simulated and investigated impinging jet.

Impinging jets are not restricted to single-phase flows, but they can be simulated in multiphase models. Edin & Šefko [22] set up a two-dimensional model for an impinging water jet and compared pressure and Nusselt number graphs with literature data. They considered air and water for their multiphase model. Recently, Rehman et al. [23] simulated impinging water jet in a three-dimensional geometry. They applied the VOF multiphase model alongside the standard $k-\epsilon$ turbulent model and published pressure, shear stress, velocity, volume fraction, and Nusselt number distributions.

Special characteristics of impinging jet flows have extended their applications. With the purpose of studying high speed (80-200 m/s) water jet cleaning process, Guha et al. [24] set up an experiment and a numerical model. They solved Eulerian multiphase and $k-\epsilon$ turbulent equations in a two-dimensional geometry. Also, Beaucamp et al. [25] simulated surface cleaning with a multiphase approach. Ostheimer and

Yang [26] investigated twin impinging jet flows in a three-dimensional and single-phase model. Caliskan et al. [27] investigated the effects of nozzle geometry on flow and heat transfer of multiple impinging jets by using experimental and numerical methods. With the purpose of studying nucleate boiling, impinging jet was simulated by Narumanchi et al. [28] using Eulerian multiphase equations. Bhagat and Wilson [29] conducted some experiments to study wall jet flow and its hydraulic jump.

In the current research, the hydrodynamic of a turbulent impinging jet has been studied experimentally and numerically. In the experiments, force on the target surface was derived for various Reynolds numbers from 72000 to 102000. In the numerical method, Eulerian multiphase equations alongside with different turbulent models and wall functions were solved in a three dimensional geometry. Additionally, in this research a study is done on mesh-independency of the results. By comparing the numerical results with the experiments, it could be concluded that the anisotropic Reynolds stress model was more efficient than other turbulent models in predicting the force on the target wall. Moreover, non-equilibrium wall function showed more suitable performance in simulation of impinging jet near the wall flow. In addition to these conclusions, contours and graphs of velocity, pressure, volume fraction, turbulent kinetic energy and wall shear stress are obtained and analyzed.

2. Governing equations

Two phase turbulent flow equations are derived and discussed in an interesting book written by Ishii and Tu et al. [30, 31]. The transport equations of volume average mass, momentum and turbulence fluid flow that are mainly used in the current study are derived in reference [30]. Here, the equations are mentioned.

Mass conservation equation for phase q is:

$$\nabla \cdot (\alpha_q \rho_q \vec{v}_q) = 0 \quad (1)$$

where, α is the phase volume fraction of phase is q , ρ is the density, and \vec{v} is the velocity vector,

and also $q = l, g$. The conservation of momentum equation for phase q is:

$$\begin{aligned} \nabla \cdot (\alpha_q \rho_q \vec{v}_q \vec{v}_q) = & -\alpha_q \nabla p + \nabla \cdot \bar{\tau}_q + \alpha_q \rho_q \vec{g} \\ & + \sum_{p=1}^n (K_{pq} (\vec{v}_p - \vec{v}_q)) + (\vec{F}_q \\ & + \vec{F}_{lift,q} + \vec{F}_{vm,q}) \end{aligned} \quad (2)$$

where K_{pq} is the interfacial drag force coefficient, \vec{F}_q is the external body force, $\vec{F}_{lift,q}$ is the lift force, $\vec{F}_{vm,q}$ is the virtual mass force, p is the pressure, and \vec{g} is the acceleration due to gravity. Here $\bar{\tau}_q$ is the qth phase stress-strain tensor:

$$\begin{aligned} \bar{\tau}_q = & \alpha_q \mu_q (\nabla \vec{v}_q + \nabla \vec{v}_q^T) + \alpha_q (\lambda_q \\ & - \frac{2}{3} \mu_q) \nabla \cdot \vec{v}_q \bar{I} \end{aligned} \quad (3)$$

here μ_q and λ_q are the shear stress and bulk viscosity of phase q. The mixture turbulence model represents the first extension of the single phase k- ϵ model. This model is applicable when phases are separate, for stratified (or nearly stratified) multiphase flows, and when the density ratio between phases is close to 1. In these cases, using mixture properties and mixture velocities is sufficient to capture important features of the turbulent flow. The k and ϵ equations describing this model are as follows:

$$\nabla \cdot (\rho_m \vec{v}_m k) = \nabla \cdot \left(\frac{\mu_{t,m}}{\sigma_k} \nabla k \right) + G_{k,m} - \rho_m \epsilon \quad (4)$$

Where k is the turbulent kinetic energy, ϵ is the dissipation rate, and $G_{k,m}$ is the turbulence kinetic energy production rate.

$$\begin{aligned} \nabla \cdot (\rho_m \vec{v}_m \epsilon) = & \nabla \cdot \left(\frac{\mu_{t,m}}{\sigma_\epsilon} \nabla \epsilon \right) + \frac{\epsilon}{k} (C_{\epsilon 1} G_{k,m} \\ & - C_{\epsilon 2} \rho_m \epsilon) \end{aligned} \quad (5)$$

where $C_{\epsilon 1}$, $C_{\epsilon 2}$ are constants, S_ϵ is the bubble-induced dissipation in the dissipation rate equation, and the mixture density, ρ_m , and mixture velocity, \vec{v}_m , are computed from:

$$\rho_m = \sum_{i=1}^N \alpha_i \rho_i \tag{6}$$

and,

$$\vec{v}_m = \frac{\sum_{i=1}^N \alpha_i \rho_i \vec{v}_i}{\sum_{i=1}^N \alpha_i \rho_i} \tag{7}$$

The turbulent viscosity, $\mu_{t,m}$, is computed from

$$\mu_{t,m} = \rho_m C_\mu \frac{k^2}{\varepsilon} \tag{8}$$

and the production of turbulent kinetic energy, $G_{k,m}$, is computed from:

$$G_{k,m} = \mu_{t,m} (\nabla \vec{v}_m + (\nabla \vec{v}_m)^T) : \nabla \vec{v}_m \tag{9}$$

The dispersed turbulence model is used when the concentrations of the secondary phase are dilute and the primary phase turbulence is regarded as the dominant process. The transport equation for primary phase Reynolds stresses \tilde{R}_{ij} , in the case of dispersed model is:

$$\begin{aligned} \frac{\partial}{\partial x_k} (\bar{\alpha} \rho \tilde{U}_k \tilde{R}_{ij}) = & -\bar{\alpha} \rho \left(\tilde{R}_{ik} \frac{\partial \tilde{U}_j}{\partial x_k} + \tilde{R}_{jk} \frac{\partial \tilde{U}_i}{\partial x_k} \right) \\ & + \frac{\partial}{\partial x_k} \left[\bar{\alpha} \mu \frac{\partial}{\partial x_k} (\tilde{R}_{ij}) \right] \\ & - \frac{\partial}{\partial x_k} [\bar{\alpha} \rho \overline{u_i u_j u_k}] \\ & + \bar{\alpha} p \left(\frac{\partial u_i}{\partial x_j} + \frac{\partial u_j}{\partial x_i} \right) - \bar{\alpha} \rho \varepsilon_{ij} \\ & + \Pi_{R,ij} \end{aligned} \tag{10}$$

The last term of Eq. (10), $\Pi_{R,ij}$, takes into account the interaction between the continuous and the dispersed phase turbulence.

3. Experiment setup

The diagram of experimental setup, shown in Fig. 1, includes nozzle, impingement surface, weight, and slider. Diameters of nozzle and target plate are 10 mm and 75 mm, respectively. While the impingement surface is horizontal, jet-to-plate distance is 35 mm. Water flow passing

through nozzle is calculated and noted down. The whole set of target plate and slider is hinged and has single degree of freedom rotational movement around the pivot. The location of the weight can be changed by using the slider. So with water impingement on the surface, the whole set can be aligned horizontally by adjusting weight to pivot distance (L_w).

The force of water on the target surface is calculated by measuring the L_w and the flow rate. For five times measuring the parameters with 90% certainty, the $L_w \pm 2.10$ mm for length and $Q \pm 0.150$ m³/s are calculated as bias and precision uncertainty. Also the horizontal position of the slider should be checked. Consequently, measurement of the force has low uncertainty; if this procedure is repeated in the same condition for several times, the results will be almost the same with very small percentage of difference. Eccentric of jet and the obstacle and the possibility of return of water to other side of target plate must be carefully avoided.

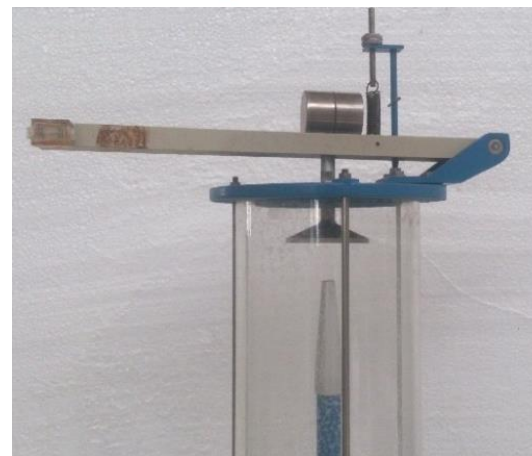
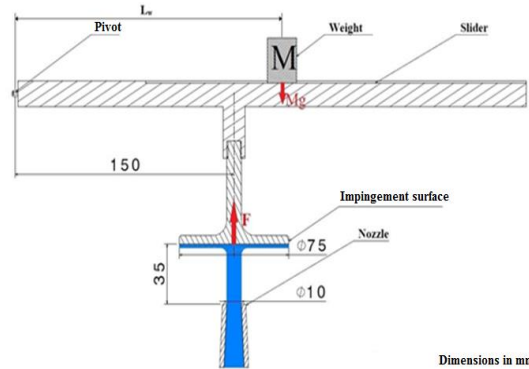


Fig. 1. Schematic diagram of the experimental setup with a picture of test rig.

Because the water flow and nozzle diameter are known, the average water velocity magnitude at nozzle exit can be calculated and named jet velocity (V_{jet}).

In a steady state condition, the whole set is fixed and momentum equilibrium equation can be used:

$$\sum_{pivot} M = 0 \tag{11}$$

Expansion of this equation reveals forces around the pivot. Therefore, the force of the water jet on the plate in the experimental method (F_{exp}) can be derived,

$$F_{exp} \times L_o = Mg \times L_w \tag{12}$$

where L_o is a constant (jet axis to pivot distance) and is equal to 150 mm. M is the mass of the weight. In this equation weights of slider and target plate are neutralized by a spring so they were removed from the equation.

Reynolds number can be defined based on jet velocity (V_{jet}) and nozzle diameter (d):

$$Re_d = \frac{\rho_w V_{jet} d}{\mu_w} \tag{13}$$

where ρ_w is water density and μ_w is water dynamic viscosity. According to the experiment situation, ρ_w and μ_w are set to 997 kg/m³ and 0.001 N.s/m², respectively.

These experiments are conducted for 6 different water flows as it was described. Results of these experiments are shown in Table 1.

4. Numerical method

4.1. Solution method

By using a finite volume based technique, transport equations can be discretized to algebraic equations that can be solved numerically. By integrating the transport equations in each control volume, this method yields discrete equations that satisfy conservation law over computational domain. Fig. 2 shows the geometry and computational mesh of this problem with the earth gravity direction. To evaluate various turbulence

weaknesses, two equations k-ε model and the five equations Reynolds Stress model are used. For near wall treatment, the standard and non-equilibrium wall functions are used. In addition, according to presence of two phases in physics of the experimental method, Eulerian-Eulerian two phase equations are solved. As it was mentioned in the introduction section, one aim of this study is to evaluate a turbulent model and wall function with the capability of predicting impinging jet flow. In this simulation, second order spatial discretization scheme for all parameters is used; except for the volume fraction equation which is based on quick scheme. The SIMPLE algorithm is used to handle pressure velocity coupling in a steady-state pressure-based numerical solution.

4.2. Computational domain and boundary conditions

Using a three-dimensional domain can extend the quality and quantity of possible studies on specifications of fluid flow.

Table 1. Experiment results.

#	L_w (mm)	Q ($\times 10^{-4} \frac{m^3}{s}$)	V_{jet} (m/s)	Re_d	F_{exp} (N)
1	93.0	5.682	7.238	72163	3.65
2	113.0	6.494	8.272	82472	4.43
3	133.0	6.711	8.550	85244	5.22
4	153.0	7.353	9.367	93389	6.00
5	173.0	7.692	9.800	97706	6.79
6	193.5	8.065	10.273	102422	7.59

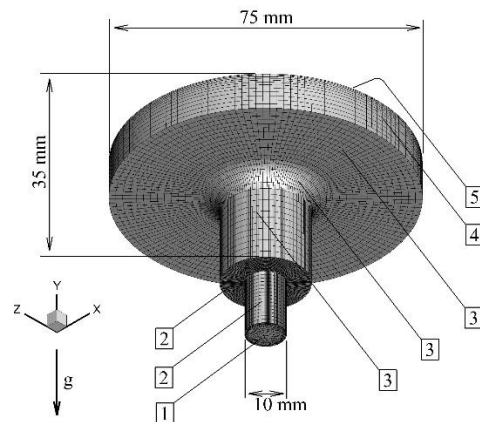


Fig. 2. Three dimensional numerical domain and mesh with boundary conditions; 1. water inlet, 2. nozzle wall, 3. air inlet, 4. outflow, 5. impingement surface (wall).

By using a three-dimensional domain, as in this study, investigating three dimensional aspects of the fluid flow will become a possible. It also provides a possibility to check the general numerical errors if the symmetry on the results is violated. This may arise by nonsymmetrical mesh or instability of turbulence or error of numerical computation and unphysical boundary conditions. Nonsymmetrical aspects on boundary conditions and body forces can be provided by considering three-dimensional geometry.

The geometry of numerical solution is created as experimental device dimensions. This three-dimensional model includes a circular water inlet (nozzle exit) with diameter of 10 mm (d) and an impingement surface with 75 mm (D) in diameter. Based on the experiment setup, distance between the nozzle and the target surface is set to 35 mm (H). As a result, in this study the jet-to-plate dimensionless distance (H/d) is equal to 3.5. This geometry is shown in Fig. 2. Using a three-dimensional domain can extend the quality and quantity of possible studies on specifications of fluid flow.

According to Table 1, velocity magnitude of water at inlet is set for 6 different velocities. At the inlet, the water volume fraction is adjusted to 1. It means that, only water permits to enter the geometry. Inlet conditions derived based on Reynolds number varied from 72000 to 102000. This range has been chosen because of the experimental device limitation. Surfaces labeled as 3 in Fig. 2, are air inlets; so water volume fraction is set to zero on them. In these boundaries, air velocity is set to zero, so that the water flow and output results will not be affected. Boundary condition for the outlet surface is set to pressure defined and its gauge pressure is set to zero. All wall conditions are adjusted as stationary and no-slip.

4.3. Mesh study

With the purpose of selecting the most suitable mesh for this work and mesh independency study, the force on the target surface was recorded at Re=91000 with different mesh size. As shown in Fig. 3, by observing that the force

remains unchanged with adding more elements, it was determined that 87000 elements are suitable to give a mesh-independent result. Consequently, using more elements does not give a different or more precise force value of the surface.

The mesh used in this simulation sets to 87000 hexahedral elements. Increased accuracy of calculations and lightened mesh are the benefits of using structured hexahedral mesh. Average value of skewness for the used mesh is 0.1. The mesh quality will be more ideal if the skewness value is nearer to zero [30]. Distance of the first node from walls is adjusted to include all used wall functions. The maximum non-dimensional distance (y^+) value is 30 for standard and non-equilibrium wall functions. It is obvious that this maximum value is located at the point where the maximum shear stress exists on the impingement surface. Also in the vicinity of the impingement region, a finer mesh was created to capture more accurately the high pressure region phenomena.

5. Results and discussion

Several numerical simulations were conducted to investigate hydrodynamic properties of impinging jets. Numerical results validation is verified by comparing these results with ones gained from the experimental method of this study. By applying different numerical models, the results are compared with experimental findings. The impingement forces on the target plate are derived for Reynolds numbers varying from 72000 to 102000. As it is shown in Fig. 1, the distance between the nozzle and the target surface is fixed.

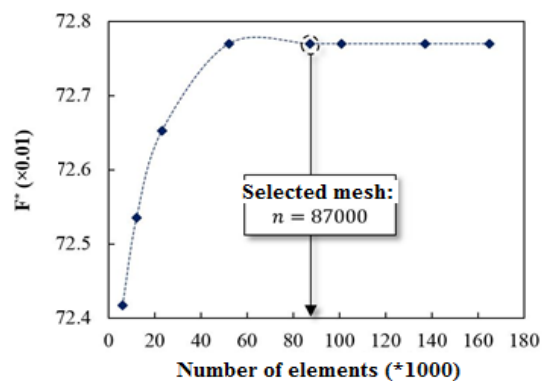


Fig. 3. Mesh-independency study.

Therefore, the jet-to-plate dimensionless distance (H/d) is constant and sets to 3.5. In order to do an efficient comparison between results, calculated forces are made normalized by dividing each force by the largest derived force. The largest force that obtained by simulation is considered as the base force so that all values of dimensionless forces may be written as:

$$F^* = \frac{F}{8.52} \tag{14}$$

where F is force and 8.52 is the largest force derived in realizable $k-\epsilon$ model in Newton. Considering Table 1., a comparison between impinging jet forces on the surface can be done. Fig. 4 shows the graph of dimensionless forces versus different Reynolds numbers for numerical and experimental results. A comparison between numerical and experimental results indicates that the Reynolds stress model, which involves anisotropic turbulent effects, alongside the non-equilibrium wall function that has a better capability in predicting the near wall phenomena, predicts flow force better than other models.

Standard wall function (SWF) is a semi-empirical function that is just valid for constant shear near wall and local equilibrium flow. Wall bounded flow with severe adverse pressure, separation, reattachment and stagnation has non-equilibrium (NE) exhibition. A wall function in turbulent flow is a remedy to avoid resolving near wall complex phenomena using predetermined functions as boundary conditions.

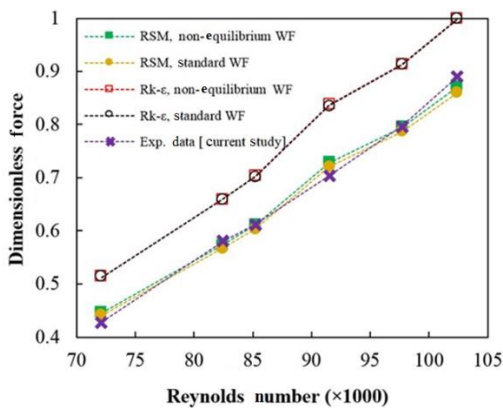


Fig. 4. Experimental and numerical force on target plate versus Reynolds numbers.

There is a gap between realizable $k-\epsilon$ model and Reynolds Stress one. The Reynolds stress model introduces different equation of velocity fluctuation correlation for each coordinates and directions; while the $k-\epsilon$ model only presents the equations of turbulent kinetic energy and its dissipation rate. Latter model considers the same value for velocity fluctuations correlation in different directions. Therefore, the five equations of Reynolds Stress model have the ability to predict the impinging jet complex flow behavior.

As a part of an engineering work, a graph of dimensionless force (F^*) versus Reynolds number for Reynolds stress turbulent model alongside non-equilibrium wall function is investigated separately. As shown in Fig. 5, a power function can be curve fitted into the force graph with a high accuracy. Hence, the forces on the target plate that are related to Reynolds numbers could be presented with this equation:

$$F^* = 2 * 10^{-11} * Re^{1.9298} \tag{15}$$

Hence, this equation can be used to predict the impingement force on a surface. Also, in future studies this equation can be studied over a wider range of Reynolds numbers. As shown in Fig. 2, instead of a symmetric geometry, a complete three-dimensional geometry is studied to control computational errors. The “ $Z=0$ plane” is introduced as a cross section for plotting contours.

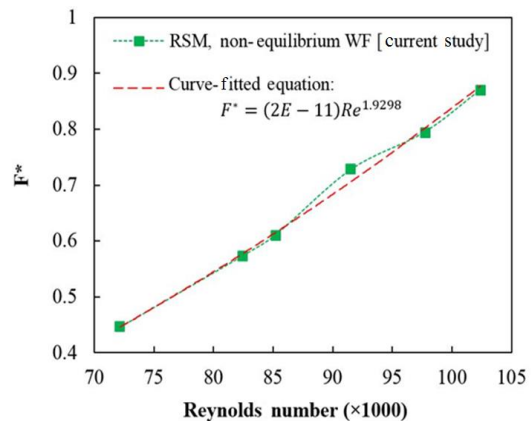


Fig. 5. Numerical force obtained from Reynolds stress model alongside non-equilibrium wall function versus Reynolds number.

This surface, as shown in Fig. 6(a), is perpendicular to target surface and includes axis of nozzle. Some flow properties were studied on this surface. All these figures are obtained by Reynolds number of 93389. In two phase flows, observing the distribution of every phase is desired. Water volume fraction is displayed in Fig. 6(b). After exiting the nozzle and forming free jet region, water flow impinges on the target plate. Then, it flows on the surface and egresses through the outlet. While the water flow spreads over the surface, water thickness decreases gradually. The presence of velocity fluctuations around the free jet causes fluctuating flow between air and water phases. Therefore, a mixture layer of both phases is created on the border of two fluids. This layer is pulled to the impingement region environs. Thickness of this film increases along the flow and is located around the impingement region as a considerable mixture layer. Since the Reynolds stress turbulent model solves the velocity fluctuation correlation equations separately, it can be an efficient model for simulating impinging jet flow and mixing effects between two phases.

With water impingement on the surface, an impingement region is formed which consists of constant pressure surfaces. Fig. 7(a) shows pressure distribution on the Z=0 plane cross section. This contour indicates that if water jet exits the nozzle at a speed of 9.36 m/s and hits a surface, it can create 50 kPa pressure increase in the center of the impingement surface. It is observed that high pressure area diameter on the target plate, which includes gauge pressure over 40 kPa, equals to nozzle diameter (d). Also, the diameter of area including pressure gradients equals to twice the nozzle diameter (2d). At Reynolds number 93389, this pressure gradient includes 50 kPa change in pressure.

Main regions of impinging jet flow can be recognized by observing velocity distribution (Fig. 7(b)) and water volume fraction distribution (Fig. 6(b)). Impingement region formation in the center of target plate causes extreme velocity gradients.

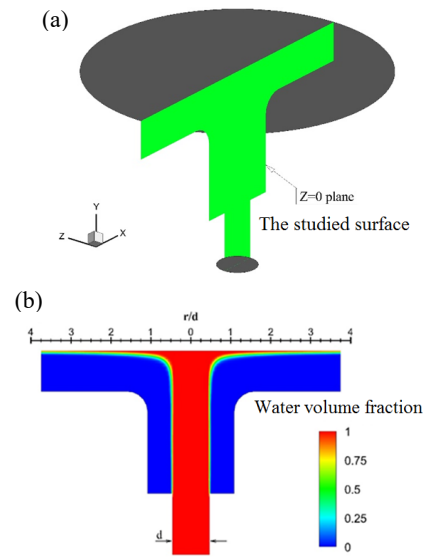


Fig. 6. (a) The z=0 plane and (b) water volume fraction distribution.

Impingement region affects the potential core and shapes it convex. So, the free jet flow impinges the surface before it fully develops. Then, the fluid flow speeds toward the radial direction in the wall jet form and exits the studied geometry through the outlet. Comparing velocity contours with pressure contours indicates that free jet flow kinetic energy converts to static pressure at stagnation region. This energy is revealed as kinetic energy at the wall jet region. Velocity vectors, in which water flow details can be observed, are shown in Fig. 8. These vectors are also plotted on the Z=0 plane. The presence of ambient static air around the water flow causes velocity gradients on the border of two fluids. Velocity changes are studied in three parts of the border. Around the free jet flow, water velocity is decreased to zero in a small distance (Fig. 8).

Such a slope does not exist on the border of impingement and wall jet region. According to Eq. (16), if velocity increases in a specific distance, shear stress between two sides will also increase,

$$\tau_{w \rightarrow a} = \mu_{eff,w} \frac{\partial V}{\partial n} \tag{16}$$

where μ_w is water effective dynamic viscosity, V is velocity magnitude, and n is the direction perpendicular to velocity direction.

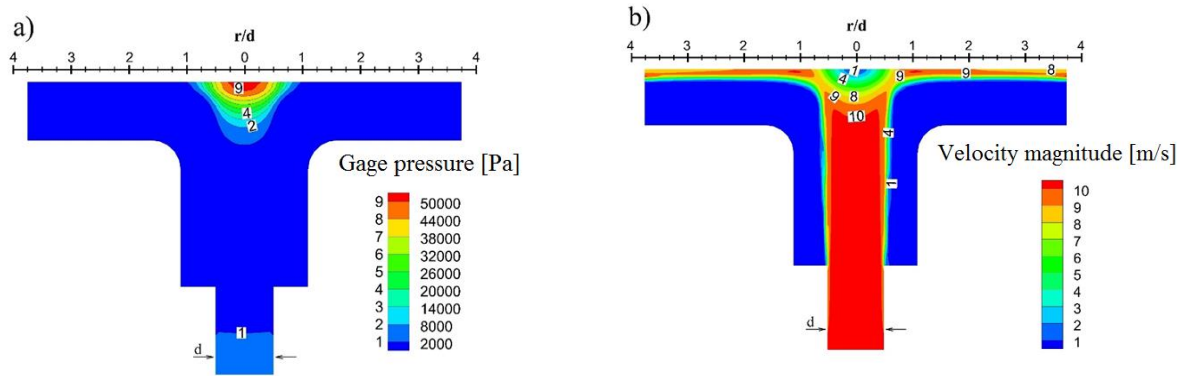


Fig. 7. Local distributions of the z=0 plane a) pressure b) velocity.

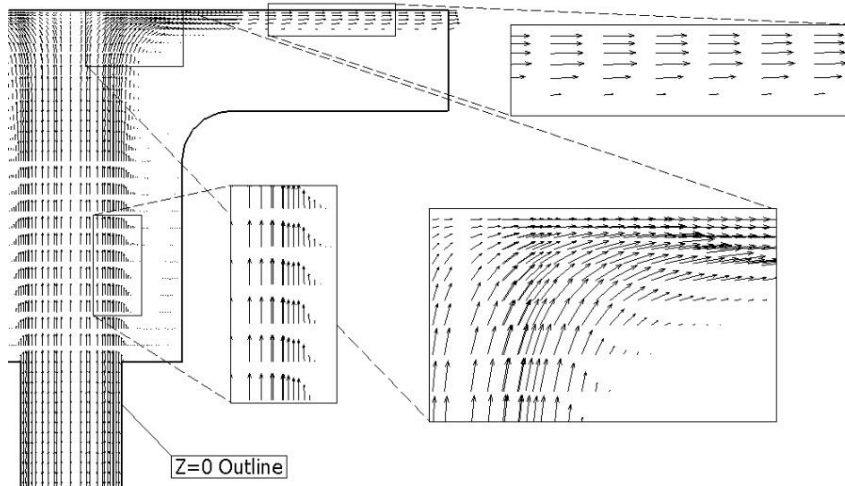


Fig. 8. Velocity vectors for water flow.

In this equation, the $\tau_{w \rightarrow a}$, indicates the shear stress applied to ambient air by water flow. As a result, it can be concluded that a considerable shear stress is applied to the mixture layer around the free jet flow. As it was stated for volume fraction contours, this shear stress drags the mixture layer to the impingement region. Furthermore, some air was taken out of geometry by the shear stress between water and air at the wall jet region.

Fig. 9 shows the turbulent kinetic energy (TKE) on the Z=0 plane, derived from the numerical method. TKE has considerable values on the border between fluids in the wall jet and the free jet regions. These high values indicate an increase in velocity fluctuations which causes mixing of water and air on the boundary of phases. As it was indicated for water volume fraction distribution (Fig. 6(b)), because of high

shear stress between air and water around the free jet flow, this mixture layer is dragged into the impingement region by the water. Also, these velocity fluctuations at the wall jet region, blend water and air to make a two-phase mixture layer. Since the Reynolds stress turbulent model solves the velocity fluctuation correlation equations separately, it can be an efficient model for simulating impinging jet flow.

When the water enters the impingement region, it loses its axial velocity and speeds toward radial direction. Consequently, the wall jet is created by water flow over the surface. As shown in Fig. 10(b), water radial velocity magnitude at the wall jet region is plotted on 6 sections. The distance of these sections are indicated relative to the nozzle's diameter (See Fig. 10(a)). While water flows on the surface, a velocity profile is formed.

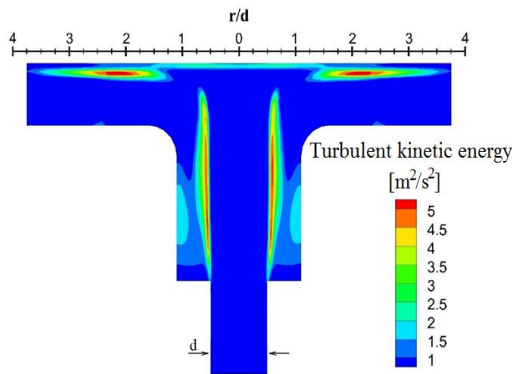


Fig. 9. Turbulent kinetic energy distribution on the z=0 plane.

The maximum velocity of this profile is located at the dimensionless distance from surface of $h/d=0.1$. Wall jet velocity profile forming indicates that the velocity changes.

The shear stress on the target plate is more severe than the shear stress of the border between air and water. Velocity gradient in the boundary of water is not constant through the flow. This gradient is higher for greater r/d values. Therefore, the shear stress between air and water increases as they reach the outflow surface.

By using numerical results, liquid film thickness on the impingement surface is plotted in Fig. 11. This graph shows the thickness of water flowing on the target plate. In addition, an equation that can fit to the thickness curve is presented as:

$$\frac{\delta}{d} = \left(\frac{0.05}{\left(\frac{r}{d} - 0.5\right)} \right) + 0.07 ; \quad (17)$$

$r/d > 0.5$

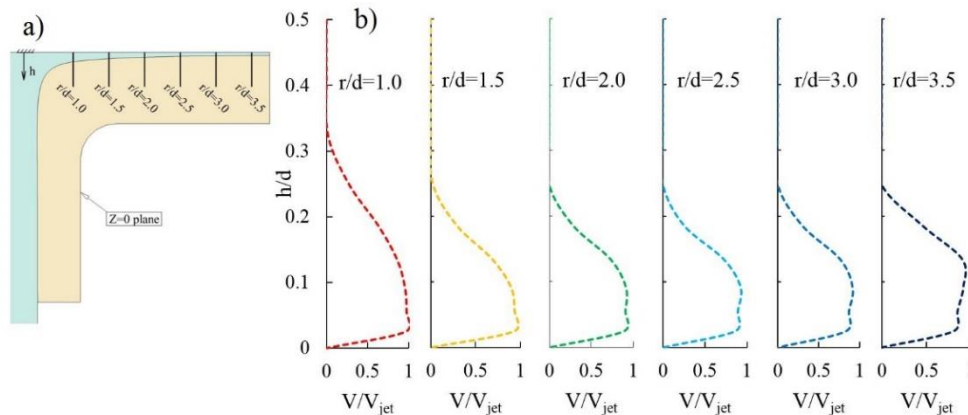


Fig. 10. Radial water flow at the wall jet region (a) location of sections (b) velocity magnitude graph.

Knowing the radial distance from nozzle axis (r), the water thickness for that point can be calculated.

While the water stream flows over the impingement surface, it applies a shear stress on the surface. Fig. 12 shows the dimensionless shear stress versus radial distance. This graph is obtained according to Reynolds number of 93389 ($V_{jet}=9.367$ m/s) by numerical results. Maximum shear stress is located at radial dimensionless distance of $r/d=0.75$. This distance includes outer parts of impingement region in which velocity and pressure gradients are considerable. As it was observed in Fig.7(a), water jet impinges the surface after exiting the nozzle and flowing through free jet region. Jet impingement on the plate decreases velocity with a high gradient. Dimensionless water velocity on the jet symmetry axis is shown in Fig. 13. As the flow approaches the surface; the velocity magnitude decreases. It is observed that, up to dimensionless distance of $h/d=1$ from the surface, water axial velocity almost equals the jet velocity. For lower values of h/d , velocity magnitude is suddenly decreased to zero which means the flow has entered the impingement region. This graph is plotted by data obtained by both turbulent models. The curve of both data is perfectly fitted on each other. Therefore, it is concluded that the derived velocity magnitudes for both models are nearly the same in vicinity of the center line.

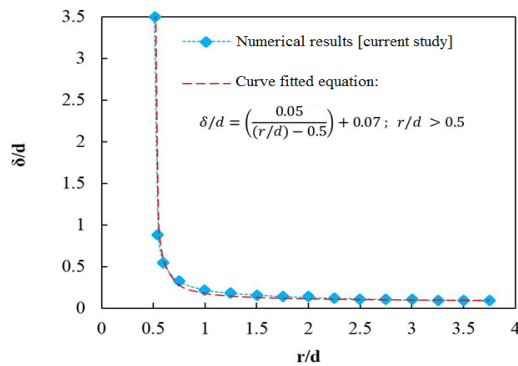


Fig. 11. Liquid film thickness on the impingement surface.

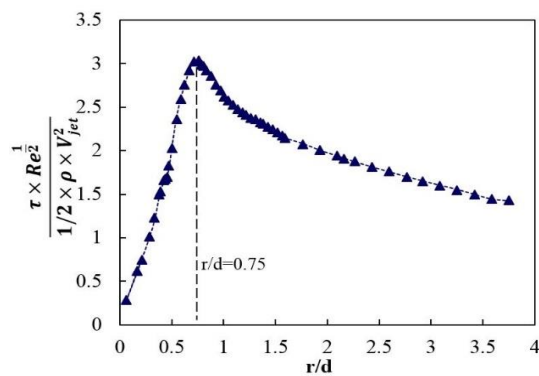


Fig. 12. Shear stress on the impingement surface.

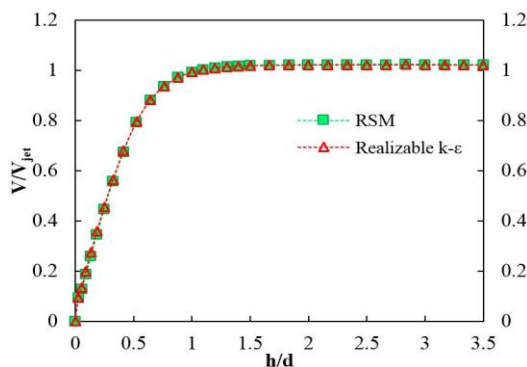


Fig. 13. Water axial velocity magnitude on axis of symmetry.

6. Conclusions

A turbulent impinging jet was investigated for different Reynolds numbers of 72000 to 102000 numerically and experimentally. The jet-to-plate dimensionless distance was set fixed and equal to 3.5. First, impingement force on the target plate was compared in both methods. Then, some properties of the jet flow were observed and investigated in different regions.

-Comparison between numerical and experimental results indicated that the Reynolds stress turbulent model alongside the non-equilibrium wall function have the capability to simulate impinging flow characteristics.

-A study was conducted on the influence of the number of mesh elements on derived force. It showed that for the number of elements higher than 87000, force on the target plate does not change. Thus, the numerical result is mesh-independent.

-By observing the pressure distribution it was concluded that high pressure area diameter on the target plate equals to nozzle diameter (d). In addition, it was observed that the diameter of area including pressure gradients equals to twice the nozzle diameter (2d).

-Shear stress between two phases in three parts of the border was observed and investigated. It was shown that this shear stress at the free jet region is higher than shear stress between phases at the other regions of the flow.

-The turbulent kinetic energy was studied on the Z=0 cross section. It indicated that there are high values of velocity fluctuations around the wall jet and free jet regions. These high values mix phases on the border and create a mixture layer of both phases. This layer is drawn out of the domain by shear stress between phases. As a result, it was concluded that because of these velocity fluctuations, the Reynolds stress model, in which velocity correlation equations are solved separately in each direction, is a suitable turbulent model to simulate multiphase impinging jets.

-By investigating the phase distribution, the graph of water thickness on the impingement surface was obtained. Besides, a practical equation was fitted on this graph.

-Shear stress on the surface of the target plate was obtained using the numerical results. This graph showed that the maximum value of shear stress is located at radial dimensionless distance of r/d=0.75.

-The axial water velocity on the jet axis was observed. It was shown that this velocity remains constant and equal to jet velocity until the flow reaches dimensionless distance of h/d=1 from the surface. Then its velocity is reduced to zero in a short distance.

References

- [1] P. S. Penumadu and A. G. Rao, "Numerical investigations of heat transfer and pressure drop characteristics in multiple jet impingement system," *Appl. Therm. Eng.*, Vol. 110, No. 1, pp. 1511-1524, (2017).
- [2] D. Cooper, D. C. Jackson, B. E. Launder and G. X. Liao, "Impinging jet studies for turbulence model assessment," *Int. J. Heat Mass Transf.*, Vol. 36, No. 10, pp. 2675-2684, (1993).
- [3] D. H. Lee, J. Song and M. C. Jo, "The effects of nozzle diameter on impinging jet heat transfer and fluid flow," *J. Heat Transfer*, Vol. 126, No. 4, p. 554, (2004).
- [4] S. V. Alekseenko and D. M. Markovich, "Electrodiffusion diagnostics of wall shear stresses in impinging jets," *J. Appl. Electrochem.*, Vol. 24, No. 7, pp. 626-631, (1994).
- [5] Y. E. Akansu, M. Sarioglu, K. Kuvvet and T. Yavuz, "Flow field and heat transfer characteristics in an oblique slot jet impinging on a flat plate," *Int. Commun. Heat Mass Transf.*, Vol. 35, No. 7, pp. 873-880, (2008).
- [6] A. Meslem *et al.*, "Flow dynamics and mass transfer in impinging circular jet at low Reynolds number. Comparison of convergent and orifice nozzles," *Int. J. Heat Mass Transf.*, Vol. 67, No. 1 pp. 25-45, (2013).
- [7] J. Stevens and B. W. Webb, "Measurements of flow structure in the stagnation impinging free-surface liquid jets," *Int. J. Heat Mass Transf.*, Vol. 36, No. 17, pp. 4283-4286, (1993).
- [8] M. Modak, K. Garg, S. Srinivasan and S. K. Sahu, "Theoretical and experimental study on heat transfer characteristics of normally impinging two dimensional jets on a hot surface," *Int. J. Therm. Sci.*, Vol. 112, No. 1, pp. 174-187, (2017).
- [9] V. Katti and S. V. Prabhu, "Experimental study and theoretical analysis of local heat transfer distribution between smooth flat surface and impinging air jet from a circular straight pipe nozzle," *Int. J. Heat Mass Transf.*, Vol. 51, No. 1, pp. 4480-4495, (2008).
- [10] M. Coussirat, J. Van Beeck, M. Mestres, E. Egusguiza, J. M. Buchlin and X. Escaler, "Computational fluid dynamics modeling of impinging gas-jet systems: I. assessment of eddy viscosity models," *J. Fluids Eng.*, Vol. 127, No. 4, pp. 691-703, (2005).
- [11] T. J. Craft, L. J. W. Graham and B. E. Launder, "Impinging jet studies for turbulence model assessment-II. An examination of the performance of four turbulence models," *Int. J. Heat Mass Transf.*, Vol. 36, No. 10, pp. 2685-2697, (1993).
- [12] N. Zuckerman and N. Lior, "Radial slot jet impingement flow and heat transfer on a cylindrical target," *J. Thermophys. Heat Transfer*, Vol. 21, No. 3, pp. 548-561, (2007).
- [13] G. Nasif, R. M. Barron and R. Balachandar, "Heat transfer due to an impinging jet in a confined space," *J. Heat Transfer*, Vol. 136, No. 11, p. 112202, (2014).
- [14] M. J. Schuler, T. Rothenfluh and P. Rudolf Von Rohr, "Stagnation flow heat transfer of confined, impinging hot water jets under supercritical pressures," *J. Supercrit. Fluids*, Vol. 99, No. 1, pp. 51-60, (2015).
- [15] M. L. Hosain, R. Bel Fdhila and A. Daneryd, "Heat transfer by liquid jets impinging on a hot flat surface," *Appl. Energy*, Vol. 164, No. 1, pp. 934-943, (2016).
- [16] M. a. Pakhomov and V. I. Terekhov, "Numerical study of fluid flow and heat transfer characteristics in an intermittent turbulent impinging round jet," *Int. J. Therm. Sci.*, Vol. 87, No. 1, pp. 85-93, (2015).
- [17] M. Shademan, R. Balachandar and R. M. Barron, "Large eddy simulation of a turbulent jet impinging on a flat plate at large stand-off distance," *Proc. of 20th Conference of the CFD Society of Canada*, Alberta, Canada, pp. 8-12, (2012).
- [18] J. Wienand, A. Riedelsheimer and B.

- Weigand, "Numerical study of a turbulent impinging jet for different jet-to-plate distances using two-equation turbulence models," *Eur. J. Mech. B/Fluids*, Vol. 61, No. 1, pp. 210-217, (2017).
- [19] Ş. M. Simionescu, N. O. Tănase, D. Broboană and C. Bălan, "Impinging air jets on flat surfaces at low reynolds numbers," *Energy Procedia*, Vol. 112, No. 1, pp. 194-203, (2017).
- [20] G. Eschmann, A. Kuntze, W. Uffrecht, E. Kaiser and S. Odenbach, "Experimental and numerical investigation of heat transfer coefficients in gaseous impinging jets-First test of a recent sensor concept for steady and unsteady flow," *Int. J. Therm. Sci.*, Vol. 96, No. 1, pp. 290-304, (2015).
- [21] Z. U. Ahmed, Y. M. Al-Abdeli and F. G. Guzzomi, "Flow field and thermal behaviour in swirling and non-swirling turbulent impinging jets," *Int. J. Therm. Sci.*, Vol. 114, No. 1, pp. 241-256, (2017).
- [22] B. Edin and Š. Šefko, "Computational modeling and simulation of nonisothermal free-surface flow of a liquid jet impinging on a heated surface," *Procedia Eng.*, Vol. 100, No. 1, pp. 115-124, (2015).
- [23] M. M. Rehman, Z. G. Qu, R. P. Fu and H. T. Xu, "Numerical study on free-surface jet impingement cooling with nanoencapsulated phase-change material slurry and nanofluid," *Int. J. Heat Mass Transf.*, Vol. 109, No. 1, pp. 312-325, (2017).
- [24] A. Guha, R. M. Barron and R. Balachandar, "An experimental and numerical study of water jet cleaning process," *J. Mater. Process. Technol.*, Vol. 211, No. 4, pp. 610-618, (2011).
- [25] A. Beaucamp, Y. Namba and R. Freeman, "Dynamic multiphase modeling and optimization of fluid jet polishing process," *CIRP Ann. - Manuf. Technol.*, Vol. 61, No. 1, pp. 315-318, (2012).
- [26] D. Ostheimer and Z. Yang, "A CFD Study of Twin Impinging Jets in a Cross-Flow," *Open Numer. Methods J.*, Vol. 4, No. 12, pp. 24-34, (2012).
- [27] S. Caliskan, S. Baskaya and T. Calisir, "Experimental and numerical investigation of geometry effects on multiple impinging air jets," *Int. J. Heat Mass Transf.*, Vol. 75, No. 1, pp. 685-703, (2014).
- [28] S. Narumanchi, A. Troshko, D. Bharathan and V. Hassani, "Numerical simulations of nucleate boiling in impinging jets: Applications in power electronics cooling," *Int. J. Heat Mass Transf.*, Vol. 51, No. 1-2, pp. 1-12, (2008).
- [29] R. K. Bhagat and D. I. Wilson, "Flow in the thin film created by a coherent turbulent water jet impinging on a vertical wall," *Chem. Eng. Sci.*, Vol. 152, No. 1, pp. 606-623, (2016).
- [30] J. Tu, K. Inthavong and K. K. L. Wong, *Computational Hemodynamis-Theory, Modelling and Applications*, Springer, (2015).
- [31] M. Ishii and T. Hibiki, *Thermo-fluid dynamics of two-phase flow*, Springer Science & Business Media, (2010).

How to cite this paper:

Hamid Reza Nazif, "Experimental study and numerical simulation of three dimensional two phase impinging jet flow using anisotropic turbulence model", *Journal of Computational and Applied Research in Mechanical Engineering*, Vol. 10, No. 1, pp. 257-269, (2020).

DOI: 10.22061/jcarme.2018.2981.1315

URL: http://jcarme.sru.ac.ir/?_action=showPDF&article=902

